Deep *Chandra* Survey of the Small Magellanic Cloud. III. Formation Efficiency of High-mass X-Ray Binaries

Vallia Antoniou[1,2] , Andreas Zezas[2,3] , Jeremy J. Drake[2] , Carles Badenes[4] , Frank Haberl[5] , Nicholas J. Wright[6] ,
Jaesub Hong[2] , Rosanne Di Stefano[2] , Terrance J. Gaetz[2] , Knox S. Long[7] , Paul P. Plucinsky[2] , Manami Sasaki[8] ,
Benjamin F. Williams[9] , and P. Frank Winkler[10]
(SMC XVP collaboration)

[1] Department of Physics and Astronomy, Box 41051, Science Building, Texas Tech University, Lubbock, TX 79409, USA
[2] Center for Astrophysics | Harvard & Smithsonian, 60 Garden Street, Cambridge, MA 02138, USA; vantoniou@cfa.harvard.edu
[3] Physics Department and Institute of Theoretical and Computational Physics, University of Crete, 71003 Heraklion, Crete, Greece; Foundation for Research and Technology-Hellas, 71110 Heraklion, Crete, Greece
[4] Department of Physics and Astronomy and Pittsburgh Particle Physics, Astrophysics and Cosmology Center, University of Pittsburgh, Pittsburgh, PA 15260, USA
[5] Max-Planck-Institut für extraterrestrische Physik, Giessenbachstrasse 1, D-85748 Garching, Germany
[6] Astrophysics Group, Keele University, Keele, ST5 5BG, UK
[7] Space Telescope Science Institute, 3700 San Martin Drive, Baltimore, MD 21218, USA
[8] Dr. Karl Remeis-Sternwarte, Erlangen Centre for Astroparticle Physics, Friedrich-Alexander-Universität Erlangen-Nürnberg, Sternwartstrasse 7, 96049 Bamberg, Germany
[9] Astronomy Department, University of Washington, Box 351580, Seattle, WA 98195, USA
[10] Department of Physics, Middlebury College, Middlebury, VT 05753, USA
Received 2019 January 2; revised 2019 September 22; accepted 2019 October 1; published 2019 December 5

Abstract

We have compiled the most complete census of high-mass X-ray binaries (HMXBs) in the Small Magellanic Cloud with the aim to investigate the formation efficiency of young accreting binaries in its low-metallicity environment. In total, we use 123 X-ray sources with detections in our *Chandra* X-ray Visionary Program (XVP), supplemented by 14 additional (likely and confirmed) HMXBs identified by Haberl & Sturm that fall within the XVP area, but are neither detected in our survey (nine sources) nor matched with any of the 127 sources identified in the XVP data (five sources). Specifically, we examine the number ratio of the HMXBs [N(HMXBs)] to (a) the number of OB stars, (b) the local star formation rate (SFR), and (c) the stellar mass produced during the specific star formation burst, all as a function of the age of their parent stellar populations. Each of these indicators serves a different role, but in all cases we find that the HMXB formation efficiency increases as a function of time (following a burst of star formation) up to ∼40–60 Myr, and then gradually decreases. The formation efficiency peaks at ∼30–40 Myr with average rates of $N(\mathrm{HMXB})\big/\mathrm{SFR} = 339^{+78}_{-83}\ (M_\odot/\mathrm{yr})^{-1}$, and $N(\mathrm{HMXB})/M_\star = (8.74^{+1.0}_{-0.92}) \times 10^{-6}\ M_\odot^{-1}$, in good agreement with previous estimates of the average formation efficiency in the broad ∼20–60 Myr age range.

Unified Astronomy Thesaurus concepts: Magellanic Clouds (990); High-mass X-ray binary stars (733); Star formation (1569); Stellar ages (1581); Early-type stars (430); X-ray point sources (1270)

1. Introduction

X-ray binaries (XRBs) are our main tool for studying the populations of compact objects in galaxies, and the formation and evolution of intermediate and higher mass binary stellar systems. Systematic studies of nearby galaxies have provided initial estimates of the formation rate of XRBs as a function of the star formation rate (SFR) and stellar mass ($M_\star$) of their host galaxies (Lehmer et al. 2010; Mineo et al. 2012). A strong dependence of the XRB formation rate on age and metallicity has been predicted (Dray 2006; Linden et al. 2010; Fragos et al. 2013); however, we are only now starting to probe the details of this connection (Shtykovskiy & Gilfanov 2005; Antoniou et al. 2010; Williams et al. 2013; Antoniou & Zezas 2016). The Small Magellanic Cloud (SMC) is the ideal target to study the dependence of the formation efficiency of XRBs on the age of their parent stellar population. It is our second nearest ($D = 61.9 \pm 0.6$ kpc; de Grijs & Bono 2015; $1' \sim 18$ pc) star-forming galaxy, and offers a clear picture of its spatially resolved star formation (SF) history (Harris & Zaritsky 2004, hereafter HZ04). Furthermore, it has low metallicity (Luck et al. 1998; Antoniou & Zezas 2016 and references therein), and hosts one of the largest populations of high-mass X-ray

binaries (HMXBs) known in a galaxy, rivaling that of the Milky Way (e.g., Coe & Kirk 2015; Haberl & Sturm 2016, hereafter HS16).

To study the HMXB populations in the SMC in detail, and in particular their connection with their parent stellar population, we performed a deep *Chandra X-ray Visionary Project (XVP)* survey of selected SMC regions (PI A. Zezas) chosen to sample stellar populations of different ages. The first results on the spectral and timing properties of pulsars detected in the survey fields are presented in Hong et al. (2016, 2017). In this work, we present our measurement of the formation efficiency of the SMC HMXB populations as a function of their age, the most detailed such measurement so far. In Section 2 we describe briefly the *Chandra* XVP SMC survey, and the source sample used, while in Section 4 we discuss the SF history of the regions studied, and we link the SF in each region with the XRB populations. In Section 6 we estimate the formation efficiency of HMXBs, and present the HMXB delay time distribution (DTD). In Section 7 we discuss these results and compare the different HMXB formation efficiency indicators. The most important findings are summarized in Section 8.
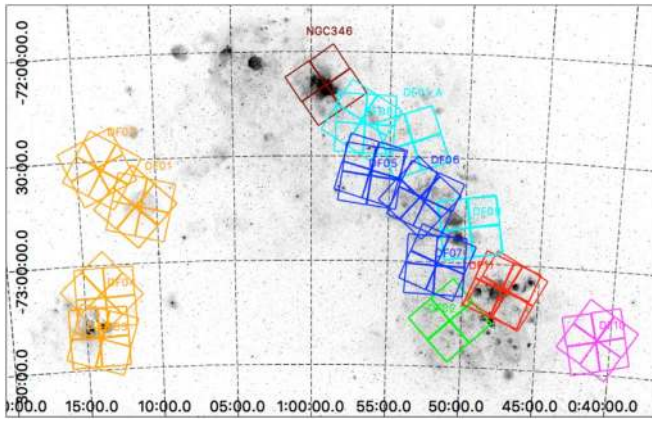
Figure 1. MCELS Hα image (F. Winkler/Middlebury College, the MCELS Team, and NOAO/AURA/NSF) overlaid with the 14 *Chandra* fields analyzed in this work, color coded for the ages of their stellar population (orange: 11 Myr, blue: 34 Myr, cyan: 42 Myr, magenta: 67 Myr). Three fields have two distinct stellar populations DF11 (7 Myr and 42 Myr—red), DF02_A (42 Myr and 167.9 Myr—green), and NGC 346 (5 Myr and 42 Myr—maroon).

Throughout this work, we adopt a distance modulus of $(m - M)_V = 18.96 \pm 0.02$ mag (de Grijs & Bono 2015), $R_V = 2.74 \pm 0.13$ (Gordon et al. 2003), and $E(B - V)$ ($=A_V/R_V$) = 0.09 ± 0.02 mag (Udalski et al. 1999), thus the extinction A_V is estimated to be 0.25 mag, and in turn[11] $A_I = 0.12$ mag, and $E(V - I) = 0.13$ mag.

2. Survey Description and Data Analysis

The SMC has been surveyed extensively in the X-ray band with *Einstein* (e.g., Seward & Mitchell 1981), *ROSAT* (e.g., Haberl et al. 2000; Sasaki et al. 2000), *RXTE* (e.g., Laycock et al. 2005; Corbet et al. 2009), *ASCA* (e.g., Yokogawa et al. 2003), and *XMM-Newton* (e.g., Haberl et al. 2012; Sturm et al. 2013), with the latter yielding the most extensive survey of the galaxy down to luminosities of 5×10^{33} erg s^{-1} (Haberl et al. 2012). These observations yielded a very rich population of HMXBs (120 sources; Haberl & Sturm 2016), while the spectroscopic and/or photometric properties of their vast majority identify them as Be/X-ray binaries (Be-XRBs; e.g., Coe & Kirk 2015). To reach well within the regime of the X-ray emission of quiescent XRBs ($\sim 10^{32}$ erg s^{-1}) and obtain as complete a picture of its HMXB populations as possible, we have been awarded a *Chandra* XVP Program to perform a comprehensive survey of 11 fields, to a depth of 100 ks exposure, selected to represent young (<100 Myr) stellar populations of different ages. These observations were performed from 2012 December to 2014 February, utilizing the ACIS-I imaging mode.

In addition, we also analyzed three archival observations reaching the same 100 ks depth. Two of these fields (PI A. Zezas; observed in 2006) overlap partially with fields from the XVP survey, and the third is centered on NGC 346 (PI M. Corcoran; observed in 2001). Although analyses of these data have been presented elsewhere (Laycock et al. 2010, and Nazé et al. 2002, respectively), for consistency we opted to reanalyze them. In Figure 1 we present a Magellanic Cloud Emission Line Survey (MCELS) Hα image of the SMC showing the observed fields, color coded for the age of their stellar population derived using data from HZ04 (for details, see Section 4).

Source detection employed *CIAO 4.5* (Fruscione et al. 2006) WAVDETECT in four bands (broad 0.5–7.0 keV, soft 0.5–1.2 keV, medium 1.2–2.0 keV, and hard 2.0–7.0 keV) on all individual ObsIDs and the merged data set for each field. All subsequent data analysis steps (source photometry, screening, spectral fitting, and timing analysis) were performed with *ACIS Extract* (AE Version 2014may23; Broos et al. 2010, 2012). This yielded 2,393 sources down to a limiting flux of 2.6×10^{-16} erg cm^{-2} s^{-1} in the full (0.5–8.0 keV) band ($\sim 50\%$ complete at 7.94×10^{-16} erg cm^{-2} s^{-1}). Further details on the survey, data analysis, and the complete source catalog[12] will be presented in V. Antoniou et al. (2020, in preparation).

3. HMXB Identification

To identify the HMXBs in the complete source catalog, we cross-correlated the locations of the 2,393 X-ray sources with the OGLE-III catalog of stars in the SMC (Udalski et al. 2008). We used a cross-correlation radius based on the relative error of the X-ray source position estimated from Equation (5) of Hong et al. (2005). We set a conservative minimum radius of $1''$ based on the minimum combined positional uncertainty of the X-ray and optical catalogs, and the standard *Chandra* boresight error ($0''8$ rms; 90% confidence[13]) Following Antoniou et al. (2010) and Antoniou & Zezas (2016), we classified as HMXBs X-ray sources with optical counterparts within the OB-star locus of the $(V, V - I)$ color–magnitude diagram (CMD). This locus is based on the location of massive stars from the spectroscopic census of the SMC (Bonanos et al. 2010). To account for the well-known effect that Be-XRBs (the most numerous subclass of SMC HMXBs) appear redder than OB stars due to the circumstellar disk of their Oe/Be star companions (e.g., Antoniou et al. 2009a, 2009b; Bonanos et al. 2010), we extended the locus to redder colors based on the location of all 120 known HMXBs from HS16 on the same CMD. We define the "extended" OB-star locus (hereafter referred to simply as the OB-star locus) to lie within $V \leqslant 18$ mag, $I \leqslant 18$ mag, and $-0.4 \leqslant V - I \leqslant 0.6$ mag (Figure 2). In total, we have identified 3,938 OGLE-III matches for the 2,393 final *Chandra* XVP sources (V. Antoniou et al. 2020, in preparation).

To estimate the chance coincidence probability of identifying spurious matches from the OGLE-III catalog as the optical counterparts of the HMXBs, we performed extensive Monte Carlo simulations following Antoniou et al. (2009b), and Antoniou & Zezas (2016). These results indicate that for a search radius of $1''$, about 10% of the bright blue ($V \leqslant 16$ mag and $-0.4 \leqslant (V - I) \leqslant 0.6$ mag) matches are spurious associations, with this probability increasing to 17% and 79% for $16 < V \leqslant 17$ mag, and $17 < V \leqslant 18$ mag, respectively (V. Antoniou et al. 2020, in preparation). These results show that the brightest (and subsequently bluest, for objects of similar brightness) match for sources with multiple matches is the most likely optical counterpart (see Antoniou et al. 2009b).

Using the above criteria, the HMXB sample consists of 127 candidate sources, identified in this work on the basis of their association with an early-type star and/or a known HMXB. Since XRBs are highly variable sources, in order to obtain a more complete picture of their population, they were

---

[11] Assuming the extinction curve of Cardelli et al. (1989).

[12] The limit we set on the probability of these sources of being just a background fluctuation—value of PROB_NO_SOURCE or P_B in *AE*—is 0.01.
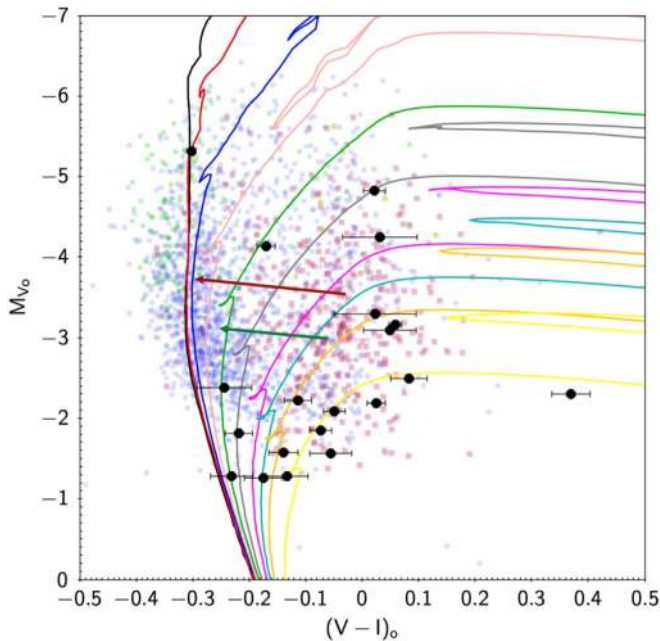[13] http://cxc.harvard.edu/cal/ASPECT/celmon/

Figure 2. Example of the age determination for the HMXBs identified in field DF11 of the *Chandra* XVP survey. The extinction-corrected magnitude and color are defined as $M_{V_o} = (m - M)_V - A_V = V - 18.96 - 0.25$, and $(V - I)_o = (V - I) - E(V - I) = (V - I) - 0.13$, respectively. The underlying points are from the spectroscopic census of OB stars in the SMC (blue B stars; green O stars, red Be stars, orange Oe stars) by Bonanos et al. (2010), overlaid with the PARSEC isochrones (black 4.5 Myr; red 6.3 Myr; blue 10.0 Myr; pink 15.8 Myr; green 25.1 Myr; gray 39.8 Myr; magenta 63.1 Myr; cyan 79.4 Myr; orange 100.0 Myr; yellow 158.5 Myr). The two vectors, maroon and dark green, show the shift of the Be stars due to their intrinsic reddening with respect to the B stars in the [B0,B2] and [B2,B4] spectral-type bins, respectively (the start and end points of the arrows are centered at the median M_{V_o} and $(V - I)_o$ values of each population).

supplemented by all additional HMXBs identified by HS16 (likely and confirmed sources) that fall within the XVP area, but are neither detected in our survey (nine sources) nor matched with any of the 127 sources identified in the XVP data (five sources). Based on the X-ray colors reported in HS16 we identified four sources with colors inconsistent with HMXBs:

1. X-ray source CXOU J011302.24-724142.1 having X-ray colors typical of a foreground star. The identified counterpart is a *Gaia* DR2 source (4687253738933765632; Gaia Collaboration et al. 2018) with a parallax and proper motion also suggestive of a nearby star.
2. X-ray source CXOU J005108.94-732144.7 being a spurious source identified as a knot in the known bright SNR IKT6.
3. X-ray source CXOU J005905.52-721035.1 being a YSO-4, i.e., an HAeBe Young Stellar Object (Ruffle et al. 2015).
4. X-ray source CXOU J010043.11-721133.6 being consistent with the anomalous X-ray pulsar (AXP) CXOU J010043.1-721134 with $P_{\rm spin} = 8.020392(9)$ s (Lamb et al. 2002, 2003; McGarry et al. 2005). No convincing optical identification was found by Durant & van Kerkwijk (2008), while the counterpart identified in this work has a ∼19% probability of being a spurious match (based on its photometry, and extensive Monte Carlo simulations; Antoniou et al. 2009b).

Based on the above findings, we exclude these four sources from the sample of the 127 candidate HMXBs identified in the *Chandra* XVP observations. Thus, our final list of candidate HMXBs consists of 137 sources. In more detail, from the comparison of the *Chandra* XVP detected sources with those listed in HS16, we found that

1. Out of the 120 high-confidence sources reported in HS16 as HMXBs, only 65 fall within the 14 *Chandra* fields used in this work. The remaining 55 HS16 HMXBs have not been covered by the *Chandra* XVP survey.
2. Out of the 65 HS16 HMXBs in the *Chandra* fields, 46 have an XVP match, i.e., 29% of the HS16 HMXBs covered by the *Chandra* survey do not have an XVP counterpart. This fraction is an indication of the number of HMXBs active at any given time.
3. Forty-one of these 46 HS16 sources have an XVP match associated with at least one OB star.
4. Five HS16 sources (12, 77, 87, 90, 117) have an XVP match, but are not associated with an OB star using the conservative minimum radius of this work.
5. From the remaining 19 HS16 HMXBs (out of the 65) that are covered by the *Chandra* XVP survey but have not been detected in that, we exclude from further consideration 5 sources that have very large positional uncertainties (>100″). Four are *RXTE* sources (HS16, #5, 17, 28, 32), and one is an *INTEGRAL* source (HS16, #8). The lack of more accurate positions for these sources does not allow us to associate them with any individual fields and hence their parent stellar populations. The remaining 14 sources supplement the 123 HMXBs identified in the *Chandra* XVP survey and comprise our final source sample of 141 candidate and confirmed HMXBs used in this work.
6. Five of these 14 HS16 sources have at least one OB counterpart in the OGLE-III catalog.
7. The minimum and maximum positional uncertainty listed for the 14 HS16 sources without an XVP match is 0″.6 and 40″.0, respectively, while regarding their spatial distribution, there are two HS16 sources within each of the DF05, DF07, DF09, DF11, and DF01_A fields, one in DF06, and 3 in DF02_A.

The optical properties of the most likely counterpart of the 123 candidate HMXBs from this work are listed in Table 1, while those of the 14 HS16 sources that supplemented our XVP sample are listed in Table 2. In particular, in Table 1 we list the HMXB ID (Column 1), along with the *Chandra* XVP field ID (Column 2), and the source ID within that particular field (Column 3). The *Chandra* catalog name appears on Column 4, followed by the R.A. and decl. (J2000.0) coordinates of each source (Columns 5 and 6), and their associated relative error (Column 7). Given that for the majority of the fields we did not find an adequate number of matches with the 2MASS catalog that would allow us to correct the absolute astrometry, we did not attempt to correct the absolute astrometry of the fields used in this work. Nonetheless, the rms error of the positions of sources in areas of the sky covered by multiple pointings is consistent with the typical absolute astrometric error of *Chandra* used in our cross-correlation.

Subsequently, in Table 1 we present the optical properties of the identified OGLE-III OB matches. The field ID, subfield ID and database number are listed in Columns 8–10, the R.A. and

4

Table 1
Optical Photometric Properties of the HMXB Sample Detected in the *Chandra* XVP Survey

HMXB	Field ID	Source	Source Name CXOU J...	R.A. (J2000.0) (deg)	Decl. (J2000.0) (deg)	Relative Error (arcsec)	OGLE-III Field	OGLE-III Subfield ID	DB_no	R.A. (J2000.0) (h m s)	Decl. (J2000.0) (° ′ ″)	V (mag)	errV	I (mag)	errI	V–I	errVI	Offset (″)
(1)	(2)	(3)	(4)	(5)	(6)	(7)	(8)	(9)	(10)	(11)	(12)	(13)	(14)	(15)	(16)	(17)	(18)	(19)
1	DF03	131	011417.74-731549.6	18.573927	−73.263799	2.40	116	3	34	01 14 17.27	−73 15 49.5	15.598	0.010	15.469	0.014	0.129	0.017	2.0
2	DF03	152	011438.26-731827.1	18.659417	−73.307544	1.12	116	3	111	01 14 38.11	−73 18 27.5	15.629	0.077	15.850	0.063	−0.221	0.099	0.7
3	DF03	212	011530.02-732043.0	18.875095	−73.345287	2.86	116	2	39	01 15 29.90	−73 20 43.4	15.049	0.024	14.943	0.031	0.106	0.039	0.6
4	DF04	64	011307.32-731140.9	18.280508	−73.194702	1.41	116	6	11258	01 13 07.17	−73 11 40.3	16.695	0.009	16.796	0.015	−0.101	0.017	0.9
5	DF04	83	011323.17-730226.3	18.346555	−73.040642	2.66	116	5	11796	01 13 22.69	−73 02 25.9	16.284	0.108	15.710	0.073	0.574	0.130	2.2
6	DF04	111	011345.88-731616.7	18.441156	−73.271316	3.44	116	6	11310	01 13 45.85	−73 16 19.8	17.370	0.017	17.481	0.024	−0.111	0.029	3.1
7	DF04	115	011350.97-731758.7	18.462381	−73.299648	4.30	116	6	11070	01 13 51.77	−73 17 57.3	14.990	0.010	15.076	0.009	−0.086	0.013	3.7
8	DF04	208	011559.90-730648.5	18.999606	−73.113484	5.34	116	4	706	01 15 59.08	−73 06 45.5	17.891	0.012	17.880	0.028	0.011	0.030	4.7
9	DF04	209	011615.39-730700.5	19.064152	−73.116813	7.96	116	4	7161	01 16 15.36	−73 07 05.1	16.803	0.008	16.903	0.014	−0.100	0.016	4.6
10	DF05	5	005418.96-722943.4	13.579012	−72.495385	3.46	105	5	24520	00 54 18.95	−72 29 43.1	17.384	0.010	17.539	0.022	−0.155	0.024	0.3
11	DF05	28	005445.57-723759.8	13.689875	−72.633302	6.30	105	6	26610	00 54 45.88	−72 37 58.4	17.787	0.013	17.878	0.031	−0.091	0.034	2.0
12	DF05	50	005514.95-723042.7	13.812295	−72.511867	2.70	105	5	31336	00 55 14.98	−72 30 42.5	16.940	0.008	17.058	0.017	−0.118	0.019	0.3
13	DF05	56	005518.40-723851.9	13.826676	−72.647751	0.39	105	6	33072	00 55 18.44	−72 38 52.0	16.022	0.027	15.711	0.029	0.311	0.040	0.2
14	DF05	80	005535.18-722906.5	13.896565	−72.485134	0.54	105	5	31235	00 55 35.14	−72 29 06.7	14.689	0.042	14.711	0.250	−0.022	0.254	0.3
15	DF05	115	005606.68-722731.7	14.027864	−72.458822	6.18	108	8	17463	00 56 06.65	−72 27 36.4	14.588	0.082	14.216	0.024	0.372	0.085	4.6
16	DF05	126	005614.64-723755.2	14.061039	−72.632002	0.34	105	6	39454	00 56 14.67	−72 37 55.3	14.536	0.018	14.307	0.062	0.229	0.065	0.1
17	DF05	135	005619.32-723503.0	14.080525	−72.584183	0.49	105	5	13010	00 56 19.30	−72 35 03.0	15.917	0.007	15.718	0.012	0.199	0.014	0.1
18	DF06	18	005131.25-724144.2	12.880224	−72.695630	4.47	101	2	7573	00 51 31.58	−72 41 48.3	17.449	0.013	17.524	0.023	−0.075	0.026	4.3
19	DF06	20	005133.10-723602.8	12.887944	−72.600788	4.67	101	2	35812	00 51 32.83	−72 36 05.2	17.695	0.019	17.758	0.044	−0.063	0.048	2.7
20	DF06	55	005209.12-723803.4	13.038032	−72.634278	0.82	101	2	14349	00 52 08.96	−72 38 03.2	15.407	0.181	15.255	0.269	0.152	0.324	0.8
21	DF06	61	005216.60-723433.1	13.069177	−72.575864	8.61	101	2	41628	00 52 15.46	−72 34 36.4	17.563	0.014	17.714	0.030	−0.151	0.033	6.2
22	DF06	153	005325.65-723606.7	13.356905	−72.601881	4.00	101	2	48243	00 53 25.20	−72 36 06.0	16.987	0.010	16.954	0.018	0.033	0.021	2.2
23	DF06	167	005336.42-723819.7	13.401752	−72.638807	1.83	101	2	22502	00 53 36.15	−72 38 21.0	17.520	0.011	17.655	0.023	−0.135	0.025	1.8
24	DF06	171	005339.74-724042.7	13.415623	−72.678531	1.67	101	2	21977	00 53 39.70	−72 40 42.4	14.994	0.015	14.805	0.049	0.189	0.051	0.4
25	DF06	193	005408.52-724343.3	13.535511	−72.728712	2.05	105	6	366	00 54 08.34	−72 43 42.0	17.429	0.013	17.596	0.023	−0.167	0.026	1.6
26	DF06	208	005455.98-724511.1	13.733254	−72.753103	0.58	105	7	34184	00 54 55.88	−72 45 10.8	15.003	0.007	14.784	0.015	0.219	0.017	0.6
27	DF07	19	005011.26-730025.5	12.546926	−73.007092	0.47	100	3	36998	00 50 11.25	−73 00 26.0	15.212	0.100	15.207	0.085	0.005	0.131	0.5
28	DF07	24	005026.80-725342.7	12.611673	−72.895191	3.33	100	4	38075	00 50 27.50	−72 53 43.9	17.120	0.010	17.197	0.018	−0.077	0.021	3.3
29	DF07	47	005057.12-731007.7	12.738000	−73.168813	0.74	100	2	31321	00 50 57.13	−73 10 08.1	14.522	0.007	14.403	0.009	0.119	0.011	0.4
30	DF07	59	005107.39-730706.9	12.780823	−73.118585	2.67	100	3	9690	00 51 07.28	−73 07 08.7	17.738	0.016	17.890	0.029	−0.152	0.033	1.9
31	DF07	169	005220.21-730731.6	13.084229	−73.125462	3.21	100	3	20108	00 52 19.93	−73 07 32.4	17.270	0.010	17.381	0.020	−0.111	0.022	1.4
32	DF07	184	005230.80-730157.4	13.128350	−73.032636	0.97	100	3	56408	00 52 30.82	−73 01 57.6	17.062	0.009	17.161	0.016	−0.099	0.018	0.1
33	DF07	227	005311.38-725320.7	13.297439	−72.889106	4.10	100	4	63614	00 53 10.88	−72 53 18.9	17.910	0.015	17.936	0.033	−0.026	0.036	2.9
34	DF07	236	005324.69-725945.8	13.352886	−72.996072	4.50	100	3	65784	00 53 24.64	−72 59 45.5	17.372	0.010	17.056	0.015	0.316	0.018	0.4
35	DF07	243	005332.25-730836.1	13.384403	−73.143382	9.14	100	2	57799	00 53 31.50	−73 08 36.3	14.829	0.006	15.123	0.009	−0.294	0.011	3.3
36	DF08	21	005510.70-721741.0	13.794616	−72.294747	6.92	108	7	7678	00 55 10.04	−72 17 43.6	17.302	0.010	17.287	0.019	0.015	0.021	3.9
37	DF08	33	005527.98-722515.7	13.866611	−72.421044	3.69	108	8	9439	00 55 28.57	−72 25 14.2	17.764	0.015	17.847	0.03	−0.083	0.034	3.1
38	DF08	41	005535.33-721512.1	13.897224	−72.253379	5.04	108	7	14990	00 55 35.30	−72 15 11.9	16.807	0.013	16.78	0.017	0.027	0.021	0.3
39	DF08	46	005539.97-721606.0	13.916543	−72.268346	2.29	108	7	15210	00 55 39.82	−72 16 04.5	17.646	0.015	17.678	0.026	−0.032	0.030	1.7
40	DF08	56	005546.75-722806.9	13.944818	−72.468587	4.10	105	5	31700	00 55 46.39	−72 28 05.3	17.849	0.013	17.771	0.026	0.078	0.029	2.3
41	DF08	62	005549.85-722709.0	13.957710	−72.452504	3.13	105	5	32582	00 55 49.83	−72 27 10.4	17.725	0.018	17.836	0.029	−0.111	0.034	1.4
42	DF08	73	005556.08-721313.5	13.983699	−72.220437	4.10	108	7	43206	00 55 55.50	−72 13 14.9	17.178	0.020	17.282	0.017	−0.104	0.019	3.0
43	DF08	90	005605.50-722159.6	14.022942	−72.366564	0.47	108	8	50674	00 56 05.54	−72 21 59.5	15.701	0.145	15.494	0.159	0.207	0.215	0.2
44	DF08	153	005646.27-722452.3	14.192814	−72.414552	1.52	108	8	26165	00 56 46.41	−72 24 53.7	15.763	0.024	15.576	0.044	0.187	0.050	1.4
45	DF08	187	005702.12-722555.8	14.258835	−72.432193	0.33	108	8	26225	00 57 02.19	−72 25 55.4	15.993	0.011	15.960	0.033	0.033	0.035	0.6
46	DF08	196	005708.99-721635.1	14.287491	−72.276439	0.48	108	7	22334	00 57 09.13	−72 16 35.2	15.260	0.013	15.090	0.014	0.170	0.019	0.6
47	DF08	201	005710.48-722135.1	14.293673	−72.359777	0.80	108	8	58268	00 57 10.57	−72 21 35.6	16.194	0.009	15.943	0.010	0.251	0.013	0.6
48	DF08	232	005723.89-722357.2	14.349559	−72.399242	0.41	108	8	26185	00 57 23.96	−72 23 56.6	14.771	0.014	14.845	0.050	−0.074	0.052	0.7
49	DF08	247	005735.92-721934.0	14.399698	−72.326131	0.34	108	1	27992	00 57 35.99	−72 19 34.2	16.008	0.014	15.806	0.023	0.202	0.027	0.3

Table 1
(Continued)

HMXB	Field ID	Source	Source Name CXOU J...	R.A. (J2000.0) (deg)	Decl. (J2000.0) (deg)	Relative Error (arcsec)	OGLE-III Field	Subfield ID	DB_no	R.A. (J2000.0) (h m s)	Decl. (J2000.0) (° ′ ″)	V (mag)	errV (mag)	I (mag)	errI (mag)	V–I (mag)	errVI (mag)	Offset (″)
(1)	(2)	(3)	(4)	(5)	(6)	(7)	(8)	(9)	(10)	(11)	(12)	(13)	(14)	(15)	(16)	(17)	(18)	(19)
50	DF08	263	005749.86-721906.4	14.457763	−72.318464	2.01	108	1	28133	00 57 49.88	−72 19 05.9	17.276	0.013	17.249	0.019	0.027	0.023	0.6
51	DF08	270	005758.43-722229.3	14.493495	−72.374833	0.40	108	1	28028	00 57 58.52	−72 22 29.1	15.788	0.074	15.846	0.067	−0.058	0.100	0.5
52	DF08	281	005819.07-722808.1	14.579472	−72.468919	8.22	105	4	19222	00 58 17.98	−72 28 04.1	15.846	0.006	15.916	0.008	−0.070	0.010	6.4
53	DF09	10	004757.06-725647.4	11.987750	−72.946510	4.62	100	5	6888	00 47 56.76	−72 56 44.7	15.770	0.005	15.774	0.008	−0.004	0.009	3.0
54	DF09	75	004903.31-725051.8	12.263827	−72.847741	0.33	100	5	44537	00 49 03.35	−72 50 52.4	16.898	0.026	16.686	0.027	0.212	0.037	0.6
55	DF09	94	004911.43-724936.9	12.297641	−72.826929	0.30	101	8	21127	00 49 11.45	−72 49 37.5	15.608	0.339	15.384	0.410	0.224	0.532	0.6
56	DF09	138	004944.24-725209.7	12.434342	−72.869371	0.34	100	5	51388	00 49 44.42	−72 52 10.1	17.811	0.016	17.826	0.033	−0.015	0.037	0.9
57	DF09	251	005125.00-725031.6	12.854207	−72.842137	2.17	101	1	7795	00 51 25.12	−72 50 32.9	15.178	0.018	14.985	0.030	0.193	0.035	1.3
58	DF10	11	003918.23-731503.8	9.825959	−73.251080	5.75	125	6	4482	00 39 18.42	−73 15 07.5	16.610	0.007	16.700	0.014	−0.090	0.016	3.7
59	DF10	275	004303.02-731628.8	10.762594	−73.274693	3.39	125	3	245	00 43 03.11	−73 16 27.2	16.602	0.009	16.703	0.016	−0.101	0.018	1.7
60	DF11	18	004544.24-730906.9	11.434373	−73.151939	4.21	125	4	22498	00 45 44.13	−73 09 07.1	14.315	0.015	14.163	0.012	0.152	0.019	0.5
61	DF11	31	004604.69-730919.4	11.519543	−73.155396	1.44	125	4	22530	00 46 04.83	−73 09 18.2	15.010	0.012	15.050	0.010	−0.040	0.016	1.4
62	DF11	46	004621.08-731020.7	11.587858	−73.172435	2.13	100	7	35194	00 46 20.87	−73 10 20.9	17.291	0.009	17.235	0.017	0.056	0.019	0.9
63	DF11	66	004632.59-730606.0	11.635816	−73.101689	0.90	100	6	4	00 46 32.63	−73 06 05.6	13.827	0.003	13.999	0.006	−0.172	0.007	0.5
64	DF11	88	004648.24-731152.6	11.701021	−73.197956	2.36	100	7	35032	00 46 47.92	−73 11 53.8	16.953	0.009	16.798	0.013	0.155	0.016	1.8
65	DF11	90	004651.14-731311.2	11.713084	−73.219781	2.89	100	7	294	00 46 51.48	−73 13 10.2	16.767	0.019	16.880	0.044	−0.113	0.048	1.8
66	DF11	108	004704.48-731537.8	11.768688	−73.260504	8.48	100	7	8857	00 47 04.89	−73 15 40.5	17.564	0.011	17.573	0.024	−0.009	0.026	3.2
67	DF11	111	004707.23-730400.8	11.780160	−73.066912	0.82	100	6	7436	00 47 07.08	−73 04 00.3	17.330	0.010	17.418	0.022	−0.088	0.024	0.9
68	DF11	125	004714.54-731122.9	11.810622	−73.189718	1.20	100	7	42667	00 47 14.51	−73 11 23.2	16.645	0.018	16.432	0.027	0.213	0.032	0.3
69	DF11	145	004722.37-730143.8	11.843230	−73.028849	3.47	100	6	38517	00 47 22.05	−73 01 46.0	17.053	0.010	16.973	0.016	0.080	0.019	2.6
70	DF11	147	004723.37-731227.3	11.847415	−73.207597	0.38	100	7	42573	00 47 23.32	−73 12 27.4	16.051	0.016	15.872	0.044	0.179	0.047	0.3
71	DF11	175	004735.01-731225.0	11.895907	−73.206940	4.25	100	7	42590	00 47 34.35	−73 12 24.2	15.979	0.006	15.791	0.009	0.188	0.011	3.0
72	DF11	227	004814.19-731003.7	12.059160	−73.167714	0.35	100	7	50768	00 48 14.10	−73 10 03.9	15.847	0.043	15.693	0.059	0.154	0.073	0.4
73	DF11	242	004834.15-730230.7	12.142323	−73.041888	0.74	100	6	45825	00 48 34.11	−73 02 31.3	14.899	0.048	14.737	0.045	0.162	0.066	0.5
74	DF11	250	004903.29-731032.4	12.263721	−73.175681	3.36	100	7	51408	00 49 03.58	−73 10 32.6	17.574	0.023	17.499	0.028	0.075	0.036	1.3
75	DF11	254	004925.71-731009.2	12.357128	−73.169244	3.82	100	7	59863	00 49 26.27	−73 10 11.0	17.881	0.015	17.926	0.031	−0.045	0.034	3.0
76	DF11	258	004946.02-731213.5	12.441763	−73.203759	17.60	100	7	58897	00 49 43.78	−73 12 20.5	16.922	0.019	16.906	0.016	0.016	0.025	12.0
77	DF01_A	3	005132.25-723101.7	12.884383	−72.517139	2.70	101	3	5523	00 51 32.46	−72 30 59.3	17.617	0.013	17.720	0.023	−0.103	0.026	2.6
78	DF01_A	13	005153.30-723148.8	12.972087	−72.530245	0.97	101	3	5189	00 51 53.14	−72 31 48.7	14.803	0.117	14.741	0.249	0.062	0.275	0.7
79	DF01_A	20	005205.73-722604.4	13.023879	−72.434562	0.79	101	3	34265	00 52 05.63	−72 26 04.2	14.927	0.017	14.794	0.042	0.133	0.045	0.5
80	DF01_A	21	005207.30-722124.9	13.030453	−72.356940	1.83	101	4	8316	00 52 07.43	−72 21 25.6	15.277	0.004	15.327	0.006	−0.050	0.007	0.8
81	DF01_A	54	005237.28-722732.7	13.155349	−72.459096	0.95	101	3	34276	00 52 37.29	−72 27 32.3	15.019	0.007	14.844	0.036	0.175	0.037	0.4
82	DF01_A	58	005245.19-722843.9	13.188314	−72.478876	1.00	101	3	11230	00 52 45.10	−72 28 43.7	14.936	0.026	14.847	0.030	0.089	0.040	0.5
83	DF01_A	68	005252.26-721715.2	13.217783	−72.287574	0.49	101	4	25552	00 52 52.23	−72 17 15.1	16.695	0.058	16.756	0.078	−0.061	0.097	0.2
84	DF01_A	105	005323.91-722715.5	13.349638	−72.454316	0.30	101	3	39681	00 53 23.86	−72 27 15.4	16.202	0.039	16.125	0.082	0.077	0.091	0.3
85	DF01_A	154	005351.56-723351.0	13.463145	−72.564187	1.86	101	2	48315	00 53 50.97	−72 33 50.3	16.851	0.008	16.939	0.013	−0.088	0.015	1.1
86	DF01_A	158	005352.55-722639.2	13.468962	−72.444250	0.51	101	3	39651	00 53 52.54	−72 26 39.1	14.980	0.019	14.989	0.071	−0.009	0.073	0.2
87	DF01_A	166	005355.37-722645.5	13.480736	−72.445979	0.37	101	3	39655	00 53 55.31	−72 26 45.3	14.831	0.079	14.757	0.097	0.074	0.125	0.4
88	DF01_A	174	005358.53-722614.8	13.493908	−72.437458	0.42	101	3	40949	00 53 58.43	−72 26 14.4	17.806	0.017	17.997	0.030	−0.191	0.034	0.7
89	DF01_A	179	005403.91-722632.9	13.516316	−72.442479	0.43	108	8	51	00 54 03.86	−72 26 32.9	15.074	0.146	15.005	0.121	0.069	0.190	0.3
90	DF01_A	192	005408.46-723207.9	13.535253	−72.535532	0.93	105	5	286	00 54 08.52	−72 32 08.8	16.996	0.008	16.969	0.027	0.027	0.028	0.9
91	DF01_A	212	005423.34-722339.7	13.597277	−72.394372	1.55	108	8	61	00 54 23.25	−72 23 39.8	15.672	0.011	15.440	0.023	0.232	0.025	0.4
92	DF01_A	241	005446.41-722522.9	13.693395	−72.423048	0.56	108	8	8650	00 54 46.37	−72 25 22.7	15.569	0.007	15.346	0.017	0.223	0.018	0.3
93	DF01_A	251	005456.26-722648.1	13.734407	−72.446681	0.51	108	8	8659	00 54 56.18	−72 26 47.8	15.443	0.059	15.327	0.094	0.116	0.111	0.4
94	DF01_A	259	005507.77-722241.1	13.782369	−72.378083	0.95	108	8	42329	00 55 07.81	−72 22 41.1	14.415	0.010	14.568	0.012	−0.153	0.016	0.2
95	DF02_A	22	004913.63-731137.8	12.306804	−73.193831	0.53	100	7	58825	00 49 13.61	−73 11 37.8	16.555	0.010	16.320	0.043	0.235	0.044	0.1
96	DF02_A	34	004929.77-731057.8	12.374044	−73.182717	0.49	100	7	58770	00 49 29.80	−73 10 58.4	16.249	0.018	15.950	0.018	0.299	0.025	0.6
97	DF02_A	44	004942.02-732314.6	12.425107	−73.387404	0.45	100	8	22235	00 49 42.01	−73 23 14.6	14.876	0.046	14.615	0.069	0.261	0.083	0.1
98	DF02_A	48	004945.96-731753.1	12.441517	−73.298109	2.08	100	8	53429	00 49 45.62	−73 17 52.9	17.449	0.014	17.513	0.023	−0.064	0.027	1.5

Table 1
(Continued)

HMXB	Field ID	Source	Source Name CXOU J...	R.A. (J2000.0) (deg)	Decl. (J2000.0) (deg)	Relative Error (arcsec)	OGLE-III Field	OGLE-III Subfield ID	DB_no	R.A. (J2000.0) (h m s)	Decl. (J2000.0) (° ′ ″)	V (mag)	errV (mag)	I (mag)	errI (mag)	V–I (mag)	errVI (mag)	Offset (″)
(1)	(2)	(3)	(4)	(5)	(6)	(7)	(8)	(9)	(10)	(11)	(12)	(13)	(14)	(15)	(16)	(17)	(18)	(19)
99	DF02_A	77	004959.84-730857.1	12.499339	−73.149210	4.22	100	7	58940	00 50 00.59	−73 08 57.7	17.286	0.013	16.876	0.017	0.410	0.021	3.3
100	DF02_A	78	005000.13-731937.3	12.500565	−73.327041	1.70	100	8	53538	00 50 00.22	−73 19 37.2	17.603	0.011	17.496	0.021	0.107	0.024	0.4
101	DF02_A	85	005004.50-731427.2	12.518759	−73.240903	1.48	100	7	26034	00 50 04.46	−73 14 27.1	15.672	0.009	15.742	0.016	−0.070	0.018	0.2
102	DF02_A	95	005010.25-731228.9	12.542734	−73.208034	0.95	100	2	31632	00 50 10.26	−73 12 29.4	17.719	0.016	17.610	0.026	0.109	0.031	0.5
103	DF02_A	99	005012.40-731155.9	12.551667	−73.198871	1.26	100	2	31293	00 50 12.42	−73 11 56.4	15.447	0.027	15.116	0.045	0.331	0.052	0.5
104	DF02_A	113	005024.78-732223.8	12.603289	−73.373300	2.03	100	1	64	00 50 25.03	−73 22 24.9	16.727	0.148	16.170	0.088	0.557	0.172	1.5
105	DF02_A	129	005035.63-731401.8	12.648480	−73.233853	0.87	100	2	103	00 50 35.60	−73 14 02.5	16.155	0.024	15.959	0.024	0.196	0.034	0.6
106	DF02_A	130	005036.05-731739.8	12.650249	−73.294393	0.51	100	1	27768	00 50 36.11	−73 17 39.6	15.708	0.008	15.446	0.010	0.262	0.013	0.3
107	DF02_A	138	005044.70-731605.2	12.686279	−73.268131	0.29	100	2	114	00 50 44.71	−73 16 05.4	15.396	0.036	15.225	0.038	0.171	0.052	0.1
108	DF02_A	144	005046.51-731252.3	12.693821	−73.214539	2.06	100	2	49	00 50 46.92	−73 12 52.3	15.571	0.007	15.173	0.008	0.398	0.011	1.7
109	DF02_A	146	005047.77-731736.4	12.699072	−73.293463	0.69	100	1	27948	00 50 47.82	−73 17 36.6	16.558	0.019	16.420	0.021	0.138	0.028	0.2
110	DF02_A	147	005047.98-731817.9	12.699929	−73.304988	0.40	100	1	27784	00 50 47.99	−73 18 18.0	15.380	0.246	15.231	0.259	0.149	0.357	0.1
111	DF02_A	155	005051.34-731228.4	12.713958	−73.207913	1.29	100	2	31946	00 50 51.44	−73 12 27.4	17.241	0.012	17.261	0.018	−0.020	0.022	1.2
112	DF02_A	196	005105.15-731500.0	12.771492	−73.250014	0.87	100	2	64	00 51 05.11	−73 15 00.1	15.195	0.129	14.965	0.093	0.230	0.159	0.2
113	DF02_A	198	005105.65-731312.0	12.773567	−73.220007	0.70	100	2	146	00 51 05.65	−73 13 11.8	15.541	0.013	15.386	0.140	0.155	0.141	0.2
114	DF02_A	222	005117.07-731606.8	12.821166	−73.268568	0.62	100	2	8772	00 51 17.10	−73 16 06.9	15.498	0.090	15.103	0.165	0.395	0.188	0.1
115	DF02_A	255	005151.95-731033.9	12.966479	−73.176102	0.45	100	2	40390	00 51 52.02	−73 10 34.0	14.459	0.016	14.402	0.060	0.057	0.062	0.3
116	DF02_A	270	005215.46-731915.4	13.064458	−73.320945	0.62	100	1	43700	00 52 15.39	−73 19 15.4	15.872	0.063	16.003	0.129	−0.131	0.144	0.3
117	DF02_A	272	005219.25-732129.0	13.080224	−73.358081	3.87	100	1	43965	00 52 20.11	−73 21 29.0	17.556	0.011	17.539	0.023	0.017	0.025	3.7
118	NGC 346	12	005750.39-720756.2	14.459981	−72.132282	0.37	108	3	32	00 57 50.38	−72 07 56.3	15.688	0.030	15.420	0.023	0.268	0.038	0.1
119	NGC 346	66	005847.04-721301.3	14.696022	−72.217050	0.88	108	2	37473	00 58 47.06	−72 13 01.9	14.654	0.024	14.693	0.053	−0.039	0.058	0.5
120	NGC 346	71	005850.25-721713.5	14.709380	−72.287110	1.26	108	2	8019	00 58 50.22	−72 17 13.6	15.025	0.026	14.869	0.022	0.156	0.034	0.1
121	NGC 346	97	005911.47-720957.2	14.797797	−72.165901	0.53	108	2	37549	00 59 11.63	−72 09 57.7	15.123	0.005	15.293	0.008	−0.170	0.009	0.9
122	NGC 346	121	005923.44-721200.4	14.847703	−72.200129	1.11	108	2	37488	00 59 23.34	−72 12 00.7	15.004	0.027	14.981	0.060	0.023	0.066	0.6
123	NGC 346	204	010102.90-720659.3	15.262107	−72.116490	0.93	108	3	21548	01 01 02.88	−72 06 59.1	15.757	0.007	15.576	0.010	0.181	0.012	0.3

Note. The first seven columns list the X-ray source properties: (1) HMXB ID; (2) *Chandra* XVP field ID; (3) source ID within that particular field; (4) *Chandra* catalog name; (5)–(6) R.A. and decl. (J2000.0) source coordinates in degrees; (7) relative positional error in arcseconds. The remaining 12 columns list the optical source properties of the associated most likely OGLE-III OB match: (8) field ID; (9) subfield ID; (10) database number; (11)–(12) R.A. and decl. (J2000.0) source coordinates in hours, minutes, seconds, and degrees, arcminutes, arcseconds, respectively; (13) V magnitude; (14) error in V magnitude; (15) I magnitude; (16) error in I magnitude; (17) V − I color; (18) error in V − I color; (19) offset between the X-ray and optical source positions in arcseconds.

Table 2
Optical Photometric Properties of Selected HMXBs from Haberl & Sturm (2016)[a]

HMXB ID	HS16 ID	OGLE-III Field	Subfield ID	DB_no	R.A. (J2000.0) (h m s)	Decl. (J2000.0) [° ′ ″]	V (mag)	errV	I (mag)	errI	V–I (mag)	errVI	Offset (″)	Comments from HS16
(1)	(2)	(3)	(4)	(5)	(6)	(7)	(8)	(9)	(10)	(11)	(12)	(13)	(14)	(15)
124	74 = ?12	100	7	58825	00 49 13.61	−73 11 37.8	16.555	0.010	16.320	0.043	0.235	0.044	0.4	HMXB Be/X RXJ0049.2-7311 = ? SXP9.13 = AXJ0049-732
125	90	100	4	9771	00 51 59.83	−72 55 23.3	15.544	0.055	15.237	0.043	0.307	0.070	0.5	HMXB Be/X? RXJ0051.9-7255, [MA93]521?, no XMM detection
126	16	100	1	43671	00 52 13.99	−73 19 18.8	14.706	0.097	14.474	0.067	0.232	0.118	0.5	HMXB Be/X RXJ0052.1-7319
127	97	101	1	16556	00 52 52.30	−72 48 30.2	14.772	0.038	14.825	0.136	−0.052	0.141	0.5	HMXB? peculiar CXOU J005252.2-724830 = ? 2E0051.1-7304 AzV138
128	115	105	5	37304	00 56 13.83	−72 30 01.0	14.556	0.007	14.457	0.035	0.099	0.036	0.6	HMXB Be/X XMMU J005613.8-722959
129	117	105	5	37362	00 56 18.26	−72 27 58.8	15.698	0.01	15.732	0.013	−0.033	0.016	4.8	HMXB? Be/X? XMMU J005618.8-722802, Be star: NGC 330:KWBBe 224
130	77	101	8	21200	00 49 42.56	−72 48 43.0	15.541	0.006	15.621	0.008	−0.080	0.010	3.3	HMXB? CXOU J004941.43-724843.8, not in EPG10, source real?
131	87	100	4	45216	00 51 16.22	−72 50 43.3	16.308	0.012	15.97	0.021	0.338	0.024	0.6	HMXB? Be/X? RXJ0051.3-7250 [MA93]447? XMM source 17.7″ away, AGN?
132	71	100	7	16987	00 48 49.31	−73 16 24.3	14.492	0.008	14.301	0.051	0.190	0.052	1.5	HMXB? Be/X? weak *Chandra* source, not in EPG10, source real?
133	101	101	2	48103	00 53 29.31	−72 33 48.2	14.665	0.01	14.55	0.017	0.114	0.020	0.5	HMXB? Be/X? weak *Chandra* source
134	68	125	3	58446	00 45 35.86	−73 14 12.7	13.014	0.011	12.988	0.015	0.026	0.019	0.5	HMXB Be/X? RXJ0045.6-7313, [MA93]114 or AzV9?, no XMM detection
135	92	101	4	8316	00 52 07.43	−72 21 25.6	15.277	0.004	15.327	0.006	−0.050	0.007	0.4	HMXB Be/X? XMMU J005207.8-722125, SXP4.78?
136	75	100	8	53025	00 49 21.75	−73 20 06.2	16.856	0.007	16.914	0.015	−0.059	0.017	0.4	HMXB? weak *Chandra* source, blue early-type star, not in EPG10, real?
137	98	100	4	54560	00 52 59.69	−72 54 03.6	17.401	0.011	17.436	0.023	−0.035	0.025	0.4	HMXB? Be/X? XMMU J005259.4-725402, weak source in XMM survey

Note.

[a] This source sample supplements our *Chandra* XVP HMXBs (for more details see Section 3). The following info is listed: (1) HMXB ID; (2) HS16 ID. The remaining 13 columns list the optical source properties of the associated most likely OGLE-III OB match: (3) field ID; (4) subfield ID; (5) database number; (6)–(7) R.A. and decl. (J2000.0) source coordinates in hours, minutes, seconds, and degrees, arcminutes, arcseconds, respectively; (8) V magnitude; (9) error in V magnitude; (10) I magnitude; (11) error in I magnitude; (12) V − I color; (13) error in V − I color; (14) offset between the X-ray and optical source positions in arcseconds; (15) comments from HS16.

decl. (J2000.0) coordinates in Columns 11–12, and the V, I and $V - I$ photometry in Columns 13, 15 and 17, followed by their errors in Columns 14, 16 and 18, respectively. The offset between the X-ray and optical source positions is listed in arcseconds in Column 19.

For the 14 sources that supplemented the 127 candidate HMXBs identified in the XVP survey the information provided in Columns 1 and 3–14 in Table 2 is similar to that listed for the 123 candidate HMXBs from this work in Columns 1 and 8–19 of Table 1, respectively. In Table 2 we also present the HMXB ID (Column 2) and the comments on the individual sources (Column 15) from the work of HS16. Regarding the optical properties of the additional sources we did not use the optical photometry presented in HS16 (which is based on the MCPS catalog); instead for consistency with the analysis of the *Chandra* sources we adopted their counterparts in the OGLE-III survey.

4. Star Formation History

As part of the Magellanic Clouds Photometric Survey (MCPS; HZ04), the spatially resolved SF history of the SMC with a scale of $12' \times 12'$ (216.2 pc $\times$ 216.2 pc) is publicly available. The SF history in each of the *Chandra* fields we adopt is the total SF history of the $12' \times 12'$ MCPS subregions they encompass, weighted by the fraction of the area of each MCPS subregion covered by the *Chandra* field.

We note that for the purpose of measuring the formation rate of HMXBs with respect to their parent stellar populations, when an HMXB falls within two or more overlapping *Chandra* fields, we associate it with the field that has a peak of SF at a time consistent with its age (indicated in Column 4 of Table 3). This is necessary because we are measuring the SF history of each *Chandra* field. Also, for simplicity we approximate each SF episode as a sequence of Gaussian events; generally 1–3 Gaussians are adequate to reproduce the evolution of the SFR during a SF event. In Table 3 we list the SFR surface density for each burst of SF (Column 10), the area of each *Chandra* field (Column 11; the intersection area of overlapping fields is assigned to only one of those fields), the burst SF (Column 12), and the stellar mass formed during the SF episode associated with each HMXB population (Column 13). The latter is calculated by integrating the SF history during the period of the SF episode of interest in each relevant field.

5. Age Dating of HMXBs

Since our goal is to measure the formation rate of HMXBs as a function of the age of their parent stellar population, we first need to constrain the ages of the HMXBs and associate them with individual SF episodes responsible for the birth of their progenitors. Ages are derived from optical counterpart positions on the $(V, V - I)$ CMD with respect to the PARSEC isochrones (v1.2S; Bressan et al. 2012) generated by CMD[14] 2.8 for $Z = 0.004$ (Figure 2). We note that due to their circumstellar disks, the Be stars are intrinsically redder than B-type stars of the same spectral type. By comparing the $(V - I)_o$ colors of B and Be stars from the census of Bonanos et al. (2010), we have found that early [B0–B2], and mid [B2–B4) spectral-type Be stars (i.e., within the typical range of companions of known SMC HMXBs; e.g., McBride et al. 2008;

Antoniou et al. 2009a; Maravelias et al. 2014) have median values of reddening-corrected $(V - I)_o$ colors ~ 0.3 and ~ 0.2 mag redder, respectively, and V-band absolute magnitudes $M_{V_o} \sim 0.2$ and ~ 0.1 mag fainter, respectively, than B stars of the same spectral type. This systematic displacement (also obvious from the background points in Figure 2) implies that a Be system appears redder and slightly fainter than a B star due to its equatorial disk.

Furthermore, each optical counterpart is associated with a SF episode taking into account the fact that stars can be associated with a SF event that overlaps with the age range of isochrones consistent with its location on the CMD. For example, the SF history of *Chandra* field DF11 shows two prominent peaks at 7 Myr and 42 Myr (indicated in Column 4 of Tables 3 and 4). Out of the 17 HMXBs of DF11 only one X-ray source has an optical counterpart with a location on the OGLE-III $(V, V - I)$ CMD consistent with the SF burst at 7 Myr (best described by the 6.3 Myr isochrone of Figure 2), while the remaining 16 have ages consistent the peak in the SF history at 42 Myr. These 16 counterparts appear to be best described by isochrones with ages from 79.5 Myr (cyan) to 158.5 Myr (yellow), but as described above this is merely a circumstellar reddening effect. The optical counterparts of these sources have mid- to late-B spectral types (based on their magnitudes and colors) indicating much younger ages, thus their photometry needs to be corrected by at least the amount indicated with the dark green arrow in Figure 2. Although this correction is estimated for B[2, 4) spectral types, i.e., for spectral types perhaps a bit earlier than that of some of these 16 counterparts, it is the best approximation available due to the fact that the sample of late (i.e., later than B4) Be-type stars in the SMC is so small that we cannot derive a reliable reddening correction for the latest B-type stars. Assuming this reddening correction, we find ages younger than ~ 63–79 Myr (magenta and cyan isochrones, respectively), which associates them with the SF burst at ~ 42 Myr (that has a span of ~ 22 Myr; age bin #4 in Table 3).

Following this procedure, we associate each of the 137 most likely optical counterparts of the identified HMXBs with a SF episode. These results are summarized in Table 3 where we list the number of sources from each field grouped in 6 age bins. The age bins are given in Column 1. In Column 2, we list the *Chandra* field ID, while in Columns 3–5 we present the number of the major SF burst, its age and time-span (identified as the FWHM of an approximate Gaussian event; see Section 4). In Columns 6 and 8 we give the number of HMXBs and OB stars, along with their related number errors in Columns 7 and 9, respectively.

The underlying assumption in this analysis is that the HMXBs do not have significant displacements from their birthplaces, so the stellar populations in their neighborhood do probe their parent stellar populations. This assumption is supported by (a) the strong association of HMXBs with star-forming regions in the SMC (e.g., Shtykovskiy & Gilfanov 2007; Antoniou et al. 2009b); and (b) the indications that HMXBs in the SMC have similar (or smaller) kick velocities compared to HMXBs in our Galaxy (e.g., Coe 2005; Antoniou et al. 2009b, 2010; Knigge et al. 2011). The latter is also consistent with the similar distribution of orbital separations and eccentricities in SMC and Galactic HMXBs (Maravelias et al. 2014). Previous works estimated typical displacements of less than ~ 250 pc assuming a travel time of ~ 20–30 Myr

---

[14] http://stev.oapd.inaf.it/cmd

Table 3
HMXB Populations and Formation Efficiency Indicators for the Major SF Bursts of Each *Chandra* Field

Age Bin ID	Field ID	SF Burst ID	Age (Myr)	Span (Myr)	HMXBs	HMXBs Error	OBs	OBs Error	SF Burst Rate $(10^{-6}\,M_\odot\,\mathrm{yr}^{-6}\,\mathrm{arcmin}^{-2})$	Area (arcmin^2)	SF Burst Rate $(10^{-3}\,M_\odot\,\mathrm{yr}^{-1})$	$M\star$ $(10^5 M_\odot)$	SFR $(10^{-1}\,M_\odot/\mathrm{yr})^{-1}$	OBs (10^{-4})	$M\star$ $(10^{-6}M_\odot^{-1})$
(1)	(2)	(3)	(4)	(5)	(6)	(7)	(8)	(9)	(10)	(11)	(12)	(13)	(14)	(15)	(16)
1	DF11	1	7	4	1	1.0	2466	49.7	348^{+139}_{-159}	330	115^{+46}_{-53}	$3.6^{+3.0}_{-1.7}$	0.9 ± 0.9	4.1 ± 4.1	$2.8^{+3.6}_{-2.8}$
	NGC 346	1	5	2	1	1.0	2190	46.8	192^{+137}_{-187}	293	56^{+40}_{-55}	$0.7^{+0.5}_{-0.7}$	$1.8^{+2.2}_{-1.8}$	4.6 ± 4.6	$14.3^{+17.6}_{-14.3}$
2	DF01	1	11	6	0	0.0	523	22.9	109^{+31}_{-30}	343	37^{+11}_{-10}	$2.1^{+1.0}_{-0.6}$	0.0 ± 0.0	0.0 ± 0.0	0.0 ± 0.0
	DF02	1	11	6	0	0.0	257	16.0	243^{+42}_{-41}	328	80^{+14}_{-14}	$4.5^{+2.1}_{-1.2}$	0.0 ± 0.0	0.0 ± 0.0	0.0 ± 0.0
	DF03	1	11	6	5	2.2	687	26.2	220^{+31}_{-37}	330	73^{+10}_{-12}	$3.9^{+1.0}_{-0.8}$	$6.9^{+3.2}_{-3.3}$	72.8 ± 32.7	$12.8^{+6.6}_{-6.3}$
	DF04	1	11	6	4	2.0	250	15.8	175^{+26}_{-25}	324	57^{+8}_{-8}	$3.2^{+1.1}_{-0.6}$	$7.0^{+3.6}_{-3.6}$	160.0 ± 80.6	$12.5^{+7.6}_{-6.7}$
3	DF05	1	34	43	5	2.2	1631	40.4	94^{+19}_{-16}	324	30^{+6}_{-5}	$14.5^{+3.8}_{-3.0}$	$16.7^{+8.2}_{-8.0}$	30.7 ± 13.7	$3.4^{+1.8}_{-1.7}$
	DF06	1	34	36	11	3.3	3003	54.8	112^{+27}_{-21}	331	37^{+9}_{-7}	$16.0^{+5.8}_{-4.1}$	$29.7^{+11.5}_{-10.6}$	36.6 ± 11.1	$6.9^{+3.2}_{-2.7}$
	DF07	1	34	34	11	3.3	3138	56.0	136^{+33}_{-55}	309	42^{+10}_{-17}	$18.3^{+7.3}_{-8.3}$	$26.2^{+10.1}_{-13.2}$	35.1 ± 10.6	$6.0^{+3.0}_{-3.3}$
4	DF08	1	42	43	24	4.9	3981	63.1	116^{+15}_{-15}	328	38^{+5}_{-5}	$17.8^{+3.1}_{-2.4}$	$63.2^{+15.3}_{-15.3}$	60.3 ± 12.3	$13.5^{+3.6}_{-3.3}$
	DF09	1	42	28	7	2.6	1957	44.2	112^{+19}_{-20}	298	33^{+6}_{-6}	$9.4^{+3.4}_{-2.1}$	$21.2^{+8.9}_{-8.9}$	35.8 ± 13.5	$7.4^{+3.9}_{-3.3}$
	DF11	2	42	22	16	4.0	2466	49.7	161^{+28}_{-31}	330	53^{+9}_{-10}	$16.3^{+7.4}_{-4.9}$	$30.2^{+9.1}_{-9.5}$	64.9 ± 16.3	$9.8^{+5.1}_{-3.8}$
	DF01_A	1	42	30	18	4.2	2551	50.5	151^{+13}_{-13}	245	37^{+3}_{-3}	$12.8^{+2.0}_{-1.6}$	$48.6^{+12.1}_{-12.1}$	70.6 ± 16.7	$14.1^{+4.0}_{-3.8}$
	DF02_A	1	42	41	26	5.1	3111	55.8	92^{+20}_{-19}	268	25^{+5}_{-5}	$12.8^{+6.0}_{-4.6}$	$104.0^{+29.1}_{-29.1}$	83.6 ± 16.5	$20.3^{+10.3}_{-8.3}$
	NGC 346	2	42	30	5	2.2	2190	46.8	125^{+16}_{-14}	293	37^{+5}_{-4}	$11.2^{+2.9}_{-2.1}$	$13.5^{+6.3}_{-6.2}$	22.8 ± 10.2	$4.5^{+2.3}_{-2.2}$
5	DF10	1	67	29	2	1.4	790	28.1	8^{+20}_{-7}	345	3^{+7}_{-3}	$7.2^{+3.4}_{-2.2}$	$66.7^{+162.5}_{-66.7}$	25.3 ± 17.9	$2.8^{+2.4}_{-2.1}$
6	DF02_A	2	266	436	1	1.0	3111	55.8	31^{+7}_{-6}	268	8^{+2}_{-2}	$67.5^{+8.8}_{-7.3}$	$12.5^{+12.9}_{-12.5}$	3.2 ± 3.2	0.1 ± 0.1

Note. Column (1) Age bin ID (Figure 3); Column (2) *Chandra* field ID (Figure 1); Columns (3)–(5) ID, age and time-span (FWHM) of the dominant SF episode; Columns (6)–(7) Number and number error of HMXBs in each field associated with the respective SF episode; Columns (8)–(9) Number of OB stars in each *Chandra* field, and error of the total number of OB stars in each *Chandra* field; Column (10) Peak SFR of this episode in units $10^{-6}\,M_\odot\,\mathrm{yr}^{-1}\,\mathrm{arcmin}^{-2}$ (errors are based on the upper and lower SFR ranges reported by HZ04); Column (11) Area of each *Chandra* field; Column (12) Peak SFR of this episode in units $10^{-3}\,M_\odot\,\mathrm{yr}^{-1}$; Column (13) Total stellar mass ($M\star$) produced in the SF episode (based on the integration of the SFR time evolution); Columns (14)–(16) HMXB formation efficiency based on the ratio of N(HMXBs) (Column 6) to the SFR (Column 12), the N(OBs) (Column 8), and the stellar mass (Column 13) produced during the SF burst they are associated with (see Section 4).

9

Table 4
Combined HMXB Populations and Average Formation Efficiency

| Age Bin ID (1) | SF Burst | | HMXB Formation Efficiency | | |
	Age (Myr) (2)	Span (Myr) (3)	SFR $(10^{-2}\ M_\odot/\mathrm{yr})^{-1}$ (4)	OB stars (10^{-3}) (5)	$M\star$ $(10^{-6} M_\odot^{-1})$ (6)
1	6	3	0.12 ± 0.10	0.43 ± 0.30	$4.7^{+0.12}_{-0.10}$
2	11	6	0.36 ± 0.13	5.2 ± 1.8	$6.6^{+0.14}_{-0.13}$
3	34	38	$2.5^{+0.58}_{-0.64}$	3.5 ± 0.67	$5.5^{+0.70}_{-0.69}$
4	42	32	4.3 ± 0.52	5.9 ± 0.60	$12^{+0.74}_{-0.61}$
5	67	30	$6.7^{+16}_{-6.7}$	2.5 ± 1.8	$2.8^{+5.7}_{-2.8}$
6	266	436	1.3 ± 1.3	0.32 ± 0.32	$0.15^{+1.3}_{-0.15}$

Note. Column (1) Age bin ID (similar to Column 1 of Table 3); Column (2) Average age (using the values of Column 4 in Table 3) for the stellar populations in a given SF episode; Column (3) Time-span (FWHM) of the dominant SF episode; Columns (4)–(6) Average HMXB formation efficiency based on the ratio of N(HMXBs) to the SFR, the N(OBs), and the stellar mass $M\star$ (using the values of Columns (15)–(17) in Table 3) produced during the SF burst they are associated with (see Section 4).

(Antoniou & Zezas 2016; see Politakis et al. 2019), which is less than the size of the Chandra fields. This is in line with population synthesis models which show that the vast majority of the HMXBs produced assuming a flat (continuous) star formation history have travel times <10 Myr, which when convolved with the distribution of their kick velocities result in displacements of less that ~250 pc (Andrews et al. 2018).

6. HMXB Formation Efficiency

We derive three different metrics of the age-dependent formation efficiency of HMXBs in Table 3, the number of HMXBs in different ages with respect to the (a) SFR of their parent stellar population (Column 14); (b) number of OB stars, N(OBs), in their respective Chandra field (Column 15); and (c) stellar mass formed during the SF episode they are associated with (Column 16).

Then, we group together Chandra fields that have similar ages (as indicated by the different group of fields shown in Table 3; e.g., DF05, DF06, and DF07, all show a prominent peak in their SF histories at ~34 Myr), and we present the mean values in each age bin in Table 4. The age dependence of these three different tracers of the HMXB formation rate is shown in three different panels in Figure 3. The error bars in the x-axis indicate the average age range of the stellar populations in each age bin.

We find that the N(HMXBs)/SFR ratio (top left panel, black squares) increases rapidly up to ~40–60 Myr, and then gradually decreases for older stellar populations. This result is consistent with previous lower age-resolution small-scale studies (involving shallow Chandra and XMM-Newton observations), which show an increased formation efficiency of HMXBs at ages between 30 and 60 Myr (of fields across the SMC Bar) compared to younger stellar populations (SMC Wing) (Shtykovskiy & Gilfanov 2005; Antoniou et al. 2009b). On the other hand, the N(HMXBs)/N(OBs) ratio (top right panel; blue circles) shows a steep increase (by about an order of magnitude) from ~6 to 10 Myr, then a flattening up to ~60 Myr, followed by a drop (by about an order of magnitude again) for ages older than ~60 Myr. The N(HMXBs)/M★ ratio

instead (bottom panel; red triangles) remains flat up to ~60 Myr, but it decreases for later ages as well.

An alternative formulation of the time taken for the formation of a class of astronomical objects (in this case, HMXBs) from the SF event that gives rise to its progenitor stellar systems is described by the DTD. The DTD is defined as the production rate of objects as a function of time after an hypothetical brief SF burst. Badenes et al. (2015, hereafter B15) described a method to recover the DTD from an object catalog and a SF history map, and applied it to LMC planetary nebulae. Here, we apply the same method to the SMC HMXB catalog described in Section 3. The only difference with respect to the B15 analysis is that the Chandra fields we used to derive the HMXB catalog do not cover a contiguous or uniform part of the SMC, and in many cases there is only partial overlap between a given Chandra field and a specific MCPS subregion. For this reason, we multiplied the SFR of each MCPS subregion in the SF history map of HZ04 by a weight between 0 and 1, which represents the fraction of the surface area of the subregion covered by Chandra (as was also done in Section 4).

The resulting DTD is presented in Figure 4. We have used the temporal binning that offers the best compromise between DTD resolution and detection significance, given N(HMXBs) and the native resolution of the SF history map. We detect significant signal in the DTD of HMXB progenitors for stellar ages 21–53 Myr, and 53–84 Myr. Stellar populations in this age range generate ~2 × 10^{-5} HMXBs per unit stellar mass. This formation efficiency, $\Psi\, T_{\mathrm{HMXB}}$, is the product of the specific HMXB formation rate, Ψ [HMXBs yr^{-1} $M_\odot^{-1}$], and mean HMXB lifetime, T_{HMXB} [yr] —see Equations (1)–(3) and Section 2 in B15. For stellar populations younger than 21 Myr, we obtain a shallow 2σ upper limit to the HMXB formation efficiency of ~2.3 × 10^{-5} $M_\odot^{-1}$. For stellar populations older than 84 Myr, we obtain a much lower upper limit of 2.5 × 10^{-7} $M_\odot^{-1}$. This indicates that there must be a maximum delay time for HMXB formation of less than 84 Myr, but longer than 53 Myr, given the significant detection in this bin.

7. Discussion

In section Section 6 we presented an analysis of the formation efficiency of HMXBs in the SMC based on a set of deep Chandra observations of this galaxy. We calculate this based on three different indicators, (N(HMXBs)/SFR, N(HMXBs)/N(OBs), and N(HMXBs)/M★, all as a function of the age of the major associated SF burst), as well at the delay function formulation. We find that there is an increase in the formation rate for ages ≳10–20 Myr and up to 40–60 Myr followed by a decline at older ages. The three HMXB formation efficiency indicators presented in Figure 3 serve different purposes.

N(HMXBs)/N(OBs) is observationally driven, and takes into account the present-day numbers of OB stars. However, it does not take into account the donor star rejuvenation due to the first mass transfer from the initially more massive star that subsequently explodes as a SN and leaves behind a neutron star (or a black hole). Because of this rejuvenation, the system will live longer than single stars of similar mass formed during the same SF episode. This discrepancy is smaller for SF episodes of similar or longer duration compared to the lifetime of HMXB systems. Nonetheless, the N(HMXBs)/N(OBs) ratio is an indicator that can be calculated directly for any nearby
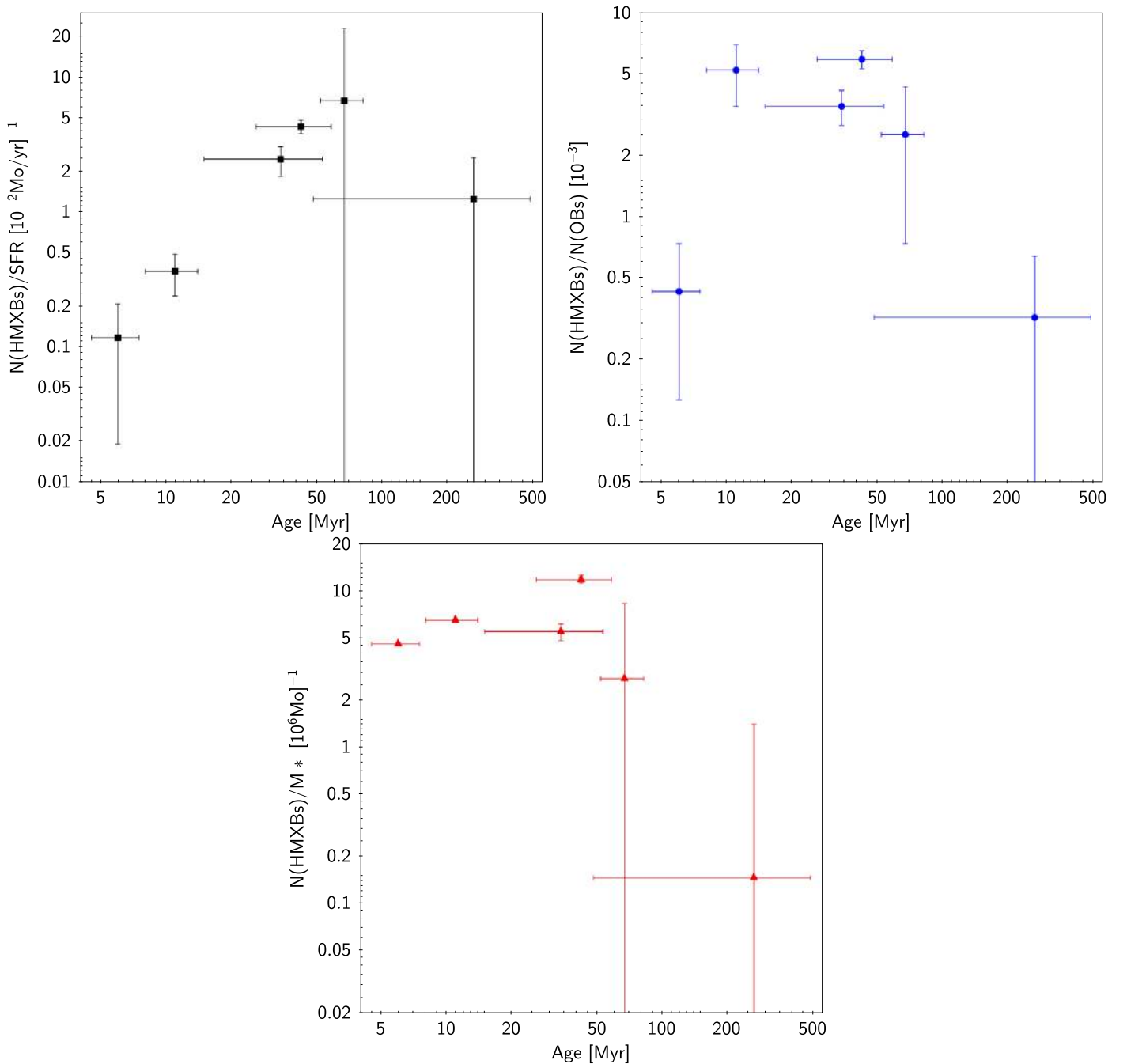
Figure 3. The following formation efficiency indicators are shown as a function of the age of their parent stellar population: (top left) N(HMXBs) over the SFR (black squares); (top right) N(HMXBs)/N(OBs) in the studied fields (blue circles); (bottom) N(HMXBs) over the stellar mass produced during the major SF burst (red triangles).

galaxy with resolved stellar populations, without the need to derive their SF history. Therefore, it serves as a useful proxy of the relative formation rate of HMXBs that can be applied to large samples of galaxies. In this work, we measured a peak formation efficiency N(HMXBs)/N(OBs) of $(5.9 \pm 0.60) \times 10^{-3}$ at 42 Myr, and an average formation efficiency in the 30–40 Myr age range of $(4.7 \pm 0.90) \times 10^{-3}$.

N(HMXBs)/SFR is based on the SF episode of the parent stellar population. It takes into account the SF event that created the binaries we observe today, but not the duration of the SF burst. In this work, we derived a peak formation efficiency N(HMXB)/SFR of $(430 \pm 52)(M_{\odot}/\text{yr})^{-1}$ at 42 Myr,

and an average formation efficiency in the 30–40 Myr age range of 339^{+78}_{-83} $(M_{\odot}/\text{yr})^{-1}$. These are in good agreement with previous estimates of the average formation efficiency in the broad $\sim$20–60 Myr age range. We also find a factor of 12 rise in the peak formation efficiency with respect to younger populations ($\sim$10 Myr) and a factor of 3 decline in older epochs ($\sim$260 Myr). The different behavior of the N(HMXBs)/SFR with respect to the N(HMXBs)/N(OBs) indicator could be the result of the age dependence of N(OBs), i.e., as the stellar populations age a smaller number of OB stars is expected to be present. From a simple stellar lifetime argument folded through the IMF, the number of OB stars will be reduced with time,
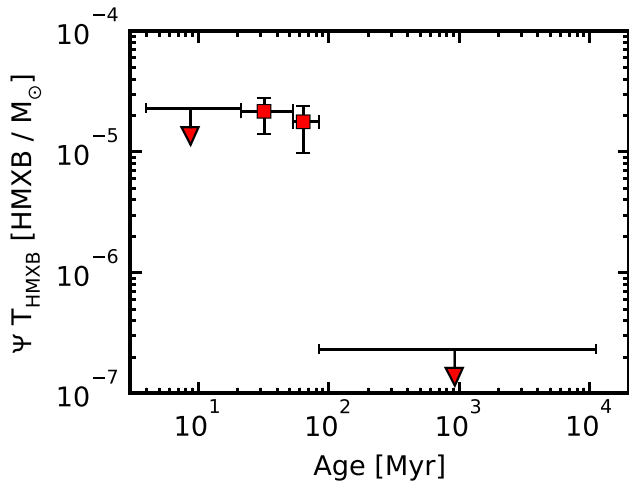
Figure 4. HMXBs delay time distribution (following B15).

while the rejuvenation of the donor star would result in a longer lifetime of the binary systems. While N(HMXBs)/SFR is considered a more accurate representation of the formation efficiency of young accreting binaries than N(HMXBs)/N (OBs), it is similarly problematic for providing observational constraints in sophisticated population synthesis models (e.g., Andrews et al. 2018).

More suitable is the ratio of N(HMXBs) to the total stellar mass produced in the relevant SF burst (N(HMXB)/$M\star$), as this takes into account the SF burst duration (the integral of the SFR as a function of time). This is the fundamental relation that we were aiming to derive from this *Chandra* XVP program, and the one that best resembles the delay function of the HMXBs. The time evolution of the HMXB formation rate normalized by the total stellar mass of their parent stellar populations is shown in the bottom panel (red points) of Figure 3. We find an increase up to ages of $\sim$30–40 Myr, followed by a sharp decline at older ages, similar to the behavior of the other two indicators. We measure a peak formation efficiency N(HMXB)/$M\star$ of $(12^{+0.74}_{-0.61}) \times 10^{-6}$ $M_\odot^{-1}$ at 42 Myr, and an average formation efficiency in the 30–40 Myr age range of $(8.74^{+1.0}_{-0.92}) \times 10^{-6}$ $M_\odot^{-1}$. The overall evolution of the N(HMXB)/$M\star$ formation efficiency (Figure 3) is consistent within the errors with the DTD (Figure 4). Moreover, our results are in good qualitative agreement with the simulated stellar mass normalized total X-ray luminosity output of a galaxy as a function of age of Fragos et al. (2013), who find an increase at ages $\gtrsim$20 Myr and a decrease at ages $\gtrsim$80 Myr. This effect becomes more prominent in metallicities like those of the SMC ($\sim$1/5 $Z_\odot$; Luck et al. 1998; Antoniou & Zezas 2016, and references therein).

The *Chandra* fields along the SMC Wing (DF01–DF04 in Figure 1) produce only a small number of HMXBs based on the surveys conducted so far (McGowan et al. 2008; this work). We attribute this deficiency on the strong but very recent ($<$10 Myr) star formation of the fields in this area (Antoniou et al. 2010) compared to the SMC Bar regions (typically $\sim$25–60 Myr). Although this deficit might indicate an elusive, young, population of HMXBs, such as highly absorbed HMXBs (e.g., Walter et al. 2015), based on XRB evolution models we would not expect a large number of XRBs at such young ages as only the few, most massive systems would have produced compact objects (Belczynski et al. 2008). Because of

the large mass of the progenitors of these systems and the low metallicity of the SMC, we would expect these systems to be predominantly black hole XRBs (Antoniou et al. 2010).

The time-resolved HMXB formation efficiency with respect to the stellar mass presented in Figure 3 is in good agreement with the general trend estimated by Shtykovskiy & Gilfanov (2007), who find a peak at similar ages ($\sim$40 Myr; albeit with coarser time resolution). We attribute differences in the absolute value of the formation efficiency between the two works to the fact that Shtykovskiy & Gilfanov (2007) consider only massive stars ($M > 8 M_\odot$) in their calculation of stellar mass that was used to normalize the number of HMXBs.

Our results are also in agreement with studies of the formation efficiency of massive Oe/Be stars in the Magellanic Clouds (e.g., Martayan et al. 2006, 2007b; Bonanos et al. 2009, 2010), and the Milky Way (McSwain & Gies 2005). These works show a peak at ages of $\sim$20–50 Myr (Iqbal & Keller 2013), matching the age of maximum production of HMXBs at least at the metallicity of the SMC. This similarity could indicate that (a) the Be stars, the donor stars of Be-XRBs (the predominant HMXB population in the SMC), are the result of binary evolution (e.g., Porter & Rivinius 2003, and references therein), and/or (b) the larger mass-loss rates of Be stars through their equatorial winds (in comparison to the much weaker spherical stellar winds) lead to an enhanced population of active XRBs (see Antoniou et al. 2010). However, only detailed population synthesis models accounting for the complex orbital evolution and mass transfer in eccentric binaries (e.g., Dray 2006) can distinguish between these possibilities.

Finally, a first assessment of the overall XRB formation rate in the LMC, which has two SF episodes at similar ages as the SMC (12.6 and 42 Myr) but with different intensities, indicates that the formation efficiency of its overall XRB population is $\sim$17 times lower than in the SMC (Antoniou & Zezas 2016). This could be the result of a metallicity effect (e.g., Be stars form more efficiently at lower metallicities as shown by Martayan et al. 2007a and Iqbal & Keller 2013). Furthermore, Dray (2006) finds that at the $\sim$1/5 $Z_\odot$ metallicity of the SMC, population synthesis models predict 3 times larger populations of HMXBs than in the Milky Way. However, only a more systematic study of the formation efficiency of XRBs in the higher metallicity LMC galaxy will show how this truly depends on the metallicity.

8. Conclusions
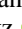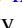
We have investigated the formation efficiency of HMXBs in the low SMC metallicity for the first time as a function of the age of their parent stellar population. We have used the different formation efficiency indicators N(HMXBs)/SFR, N(HMXBs)/N(OBs), and N(HMXBs)/$M\star$, all as a function of the age of the major associated SF burst. In all cases, we find an increase in the formation efficiency up to an age of $\sim$40–60 Myr, and a gradual decrease thereafter. In this work, we derive a peak formation efficiency N(HMXB)/SFR of (430 ± 52) $(M_\odot$/yr$)^{-1}$ at 42 Myr, and an average formation efficiency of 339^{+78}_{-83} $(M_\odot$/yr$)^{-1}$ in the 30–40 Myr age range, in good agreement with previous estimates of the average formation efficiency in the broad $\sim$20–60 Myr age range. This peak in the formation efficiency of the SMC HMXBs is 12 and 3 times higher than at earlier ($\sim$10 Myr) and later epochs ($\sim$260 Myr), respectively, and it is in excellent agreement with

previous studies that have examined it on Be stars in both the Magellanic Clouds and the Milky Way. We also measure a peak formation efficiency $N(\text{HMXBs})/N(\text{OBs})$ of $(5.9 \pm 0.60) \times 10^{-3}$ and $N(\text{HMXB})/M\star$ of $(12^{+0.74}_{-0.61}) \times 10^{-6}\ M_\odot^{-1}$ at 42 Myr. Finally, in the 30–40 Myr age range, we derive an average formation efficiency $N(\text{HMXBs})/N(\text{OBs})$ of $(4.7 \pm 0.90) \times 10^{-3}$ and $N(\text{HMXB})/M\star$ of $(8.74^{+1.0}_{-0.92}) \times 10^{-6}\ M_\odot^{-1}$.

Software: CIAO (Fruscione et al. 2006), ACIS Extract (AE Version 2014may23; Broos et al. 2010, 2012), TOPCAT (Taylor 2005), PARSEC isochrones (v1.2S; Bressan et al. 2012).

ORCID iDs

Vallia Antoniou ⬡ https://orcid.org/0000-0001-7539-1593
Andreas Zezas ⬡ https://orcid.org/0000-0001-8952-676X
Jeremy J. Drake ⬡ https://orcid.org/0000-0002-0210-2276
Carles Badenes ⬡ https://orcid.org/0000-0003-3494-343X
Frank Haberl ⬡ https://orcid.org/0000-0002-0107-5237
Nicholas J. Wright ⬡ https://orcid.org/0000-0002-8389-8711
Jaesub Hong ⬡ https://orcid.org/0000-0002-6089-5390
Rosanne Di Stefano ⬡ https://orcid.org/0000-0003-0972-1376
Terrance J. Gaetz ⬡ https://orcid.org/0000-0002-5115-1533
Knox S. Long ⬡ https://orcid.org/0000-0002-4134-864X
Paul P. Plucinsky ⬡ https://orcid.org/0000-0003-1415-5823
Manami Sasaki ⬡ https://orcid.org/0000-0001-5302-1866
Benjamin F. Williams ⬡ https://orcid.org/0000-0002-7502-0597
P. Frank Winkler ⬡ https://orcid.org/0000-0001-6311-277X

References

Andrews, J. J., Zezas, A., & Fragos, T. 2018, ApJS, 237, 1
Antoniou, V., Hatzidimitriou, D., Zezas, A., & Reig, P. 2009a, ApJ, 707, 1080
Antoniou, V., & Zezas, A. 2016, MNRAS, 459, 528
Antoniou, V., Zezas, A., Hatzidimitriou, D., & Kalogera, V. 2010, ApJL, 716, L140
Antoniou, V., Zezas, A., Hatzidimitriou, D., & McDowell, J. C. 2009b, ApJ, 697, 1695
Badenes, C., Maoz, D., & Ciardullo, R. 2015, ApJL, 804, L25
Belczynski, K., Kalogera, V., Rasio, F. A., et al. 2008, ApJS, 174, 223
Bonanos, A. Z., Lennon, D. J., Köhlinger, F., et al. 2010, AJ, 140, 416
Bonanos, A. Z., Massa, D. L., Sewilo, M., et al. 2009, AJ, 138, 1003
Bressan, A., Marigo, P., Girardi, L., et al. 2012, MNRAS, 427, 127
Broos, P., Townsley, L., Getman, K., & Bauer, F. 2012, AE: ACIS Extract, Astrophysics Source Code Library, ascl:1203.001
Broos, P. S., Townsley, L. K., Feigelson, E. D., et al. 2010, ApJ, 714, 1582
Cardelli, J. A., Clayton, G. C., & Mathis, J. S. 1989, ApJ, 345, 245
Coe, M. J. 2005, MNRAS, 358, 1379
Coe, M. J., & Kirk, J. 2015, MNRAS, 452, 969
Corbet, R. H. D., Coe, M. J., McGowan, K. E., et al. 2009, in Proc. IAU Symp. 256, The Magellanic System Stars, Gas, and Galaxies (Cambridge: Cambridge Univ. Press), 361
de Grijs, R., & Bono, G. 2015, AJ, 149, 179
Dray, L. M. 2006, MNRAS, 370, 2079
Durant, M., & van Kerkwijk, M. H. 2008, ApJ, 680, 1394
Fragos, T., Lehmer, B., Tremmel, M., et al. 2013, ApJ, 764, 41
Fruscione, A., McDowell, J. C., Allen, G. E., et al. 2006, Proc. SPIE, 6270, 62701V
Gaia Collaboration, Brown, A. G. A., Vallenari, A., et al. 2018, A&A, 616, A1
Gordon, K. D., Clayton, G. C., Misselt, K. A., Landolt, A. U., & Wolff, M. J. 2003, ApJ, 594, 279
Grimm, H.-J., Gilfanov, M., & Sunyaev, R. 2003, MNRAS, 339, 793
Haberl, F., Filipović, M. D., Pietsch, W., & Kahabka, P. 2000, A&AS, 142, 41
Haberl, F., & Sturm, R. 2016, A&A, 586, A81
Haberl, F., Sturm, R., Ballet, J., et al. 2012, A&A, 545, A128
Harris, J., & Zaritsky, D. 2004, AJ, 127, 1531
Harrison, F. A., Craig, W. W., Christensen, F. E., et al. 2013, ApJ, 770, 103
Hong, J., Antoniou, V., Zezas, A., et al. 2016, ApJ, 826, 4
Hong, J., Antoniou, V., Zezas, A., et al. 2017, ApJ, 847, 26
Hong, J., van den Berg, M., Schlegel, E. M., et al. 2005, ApJ, 635, 907
Iqbal, S., & Keller, S. C. 2013, MNRAS, 435, 3103
Knigge, C., Coe, M. J., & Podsiadlowski, P. 2011, Natur, 479, 372
Lamb, R. C., Fox, D. W., Macomb, D. J., et al. 2002, ApJL, 574, L29
Lamb, R. C., Fox, D. W., Macomb, D. J., et al. 2003, ApJL, 599, L115
Laycock, S., Corbet, R. H. D., Coe, M. J., et al. 2005, ApJS, 161, 96
Laycock, S., Zezas, A., Hong, J., Drake, J. J., & Antoniou, V. 2010, ApJ, 716, 1217
Lehmer, B. D., Alexander, D. M., Bauer, F. E., et al. 2010, ApJ, 724, 559
Lehmer, B. D., Basu-Zych, A. R., Mineo, S., et al. 2016, ApJ, 825, 7
Linden, T., Kalogera, V., Sepinsky, J. F., et al. 2010, ApJ, 725, 1984
Luck, R. E., Moffett, T. J., Barnes, T. G., III, & Gieren, W. P. 1998, AJ, 115, 605
Maravelias, G., Zezas, A., Antoniou, V., & Hatzidimitriou, D. 2014, MNRAS, 438, 2005
Martayan, C., Floquet, M., Hubert, A. M., et al. 2007a, A&A, 472, 577
Martayan, C., Frémat, Y., Hubert, A.-M., et al. 2006, A&A, 452, 273
Martayan, C., Frémat, Y., Hubert, A.-M., et al. 2007b, A&A, 462, 683
McBride, V. A., Coe, M. J., Negueruela, I., Schurch, M. P. E., & McGowan, K. E. 2008, MNRAS, 388, 1198
McGarry, M. B., Gaensler, B. M., Ransom, S. M., et al. 2005, ApJL, 627, L137
McGowan, K. E., Coe, M. J., Schurch, M. P. E., et al. 2008, MNRAS, 383, 330
McSwain, M. V., & Gies, D. R. 2005, ApJS, 161, 118
Mineo, S., Gilfanov, M., & Sunyaev, R. 2012, MNRAS, 419, 2095
Nazé, Y., Hartwell, J. M., Stevens, I. R., et al. 2002, ApJ, 580, 225
Politakis, C., Zezas, A., Andrews, J., & Williams, S. 2019, MNRAS, submitted
Porter, J. M., & Rivinius, T. 2003, PASP, 115, 1153
Ruffle, P. M. E., Kemper, F., Jones, O. C., et al. 2015, MNRAS, 451, 3504
Sasaki, M., Haberl, F., & Pietsch, W. 2000, A&AS, 147, 75
Seward, F. D., & Mitchell, M. 1981, ApJ, 243, 736
Shtykovskiy, P., & Gilfanov, M. 2005, A&A, 431, 597
Shtykovskiy, P. E., & Gilfanov, M. R. 2007, AstL, 33, 437
Sturm, R., Haberl, F., Pietsch, W., et al. 2013, A&A, 558, A3
Taylor, M. B. 2005, TOPCAT & STIL: Starlink Table/VOTable Processing Software, adass XIV (San Francisco, CA: ASP), 29
Udalski, A., Soszynski, I., Szymanski, M., et al. 1999, AcA, 49, 437
Udalski, A., Soszyński, I., Szymański, M. K., et al. 2008, AcA, 58, 329
Walter, R., Lutovinov, A. A., Bozzo, E., & Tsygankov, S. S. 2015, A&ARv, 23, 2
Williams, B. F., Binder, B. A., Dalcanton, J. J., Eracleous, M., & Dolphin, A. 2013, ApJ, 772, 12
Yokogawa, J., Imanishi, K., Tsujimoto, M., Koyama, K., & Nishiuchi, M. 2003, PASJ, 55, 161